JACS
JOURNAL OF THE AMERICAN CHEMICAL SOCIETY

Article

pubs.acs.org/JACS

Layer-by-Layer Self-Assembly of CdS Quantum Dots/Graphene Nanosheets Hybrid Films for Photoelectrochemical and Photocatalytic Applications

Fang-Xing Xiao, Jianwei Miao, and Bin Liu*

School of Chemical and Biomedical Engineering, Nanyang Technological University, 62 Nanyang Drive, Singapore 637459, Singapore

Supporting Information

ABSTRACT: In recent years, increasing interest has been devoted to synthesizing graphene−semiconductor nanocomposites as efficient photocatalysts for extensive applications. Unfortunately, it is still challenging to make uniform graphene−semiconductor composite films with controllable film thickness and architecture, which are of paramount importance to meet the application requirements. In this work, stable aqueous dispersion of polymer-modified graphene nanosheets (GNs) was prepared via in situ reduction of exfoliated graphite oxide in the presence of cationic poly(allylamine hydrochloride) (PAH). The resultant water-soluble PAH-modified GNs (GNs-PAH) in conjunction with tailor-made negatively charged CdS quantum dots (QDs) were utilized as nanobuilding blocks for sequential layer-by-layer (LbL) self-assembly of well-defined GNs−CdS QDs hybrid films, in which CdS QDs overspread evenly on the two-dimensional (2D) GNs. It was found that the alternating GNs−CdS QDs multilayered films showed significantly enhanced photoelectrochemical and photocatalytic activities under visible light irradiation as compared to pure CdS QDs and GNs films. The enhancement was attributed to the judicious integration of CdS QDs with GNs in an alternating manner, which maximizes the 2D structural advantage of GNs in GNs−CdS QDs composite films. In addition, photocatalytic and photoelectrochemical mechanisms of the GNs−CdS QDs multilayered films were also discussed. It is anticipated that our work may open new directions for the fabrication of uniform semiconductor/GNs hybrid films for a wide range of applications.

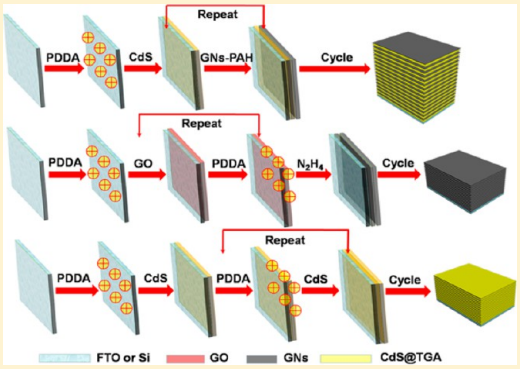

1. INTRODUCTION

Graphene, a single layer of carbon atoms densely packed in a honeycomb two-dimensional (2D) lattice,[1,2] has received great research attention both theoretically and experimentally, and triggered a scientific "gold rush" because of its unique physical and chemical properties, such as large specific surface area, high electrical conductivity, superior mechanical properties, and excellent electrochemical stability, thus making it a promising candidate for a wide range of applications, including solar cells, sensitive sensors, photocatalysis, energy conversion, and storage devices.[3−9] Particularly, graphene nanosheets (GNs) films with controllable composition and large-area uniformity are of paramount importance to meet the application requirements. Over the past few years, tremendous efforts have been devoted to developing GNs-based functional films;[10,11] synthetic routes toward GNs film nowadays are primarily centered on conventional methods including electrophoretic deposition,[12] Langmuir−Blodgett deposition,[13] vacuum filtration,[14] solution casting,[15] drop casting,[16] dip coating,[17] and spin coating.[18] While these solution approaches have succeeded in fabricating GNs-based films, it is still challenging to achieve uniform GNs film with thickness of several nanometers along with tunable control over architecture and properties.

Layer-by-layer (LbL) self-assembly, as a versatile bottom-up nanofabrication technique, exhibits prominent advantages over conventional approaches on versatility and simplicity, and furnishes molecular-level control over the thickness, structure, and composition of the multilayered films with simple benchmark operations.[19−22] Meanwhile, it should be mentioned that 2D planar morphology and negatively charged surface of GO provide new options for LbL assembly of various high-quality GNs hybrid films.[23−26] In this regard, uniform GNs-based multilayered films consisting of GNs and other ingredients can be facilely achieved by capitalizing on the substantial electrostatic interactions afforded by LbL buildup.

Recently, increasing attention has been paid to the synthesis of GNs−semiconductor nanocomposites as efficient photocatalysts, because of the 2D nanostructure and excellent electron conductivity of GNs, which can effectively separate the photogenerated charge carriers from semiconductors, and thus improve the photocatalytic activity.[27−31] Among which, GNs−CdS heterostructures have received the most attention because of the suitable band gap, size-dependent electronic, and

Received: November 15, 2013
Published: January 6, 2014

   dx.doi.org/10.1021/ja411651e | J. Am. Chem. Soc. 2014, 136, 1559−1569

Scheme 1. Schematic Illustration for LbL Self-Assembly of GNs−CdS QDs, Pure GNs, and Pure CdS QDs Multilayered Films

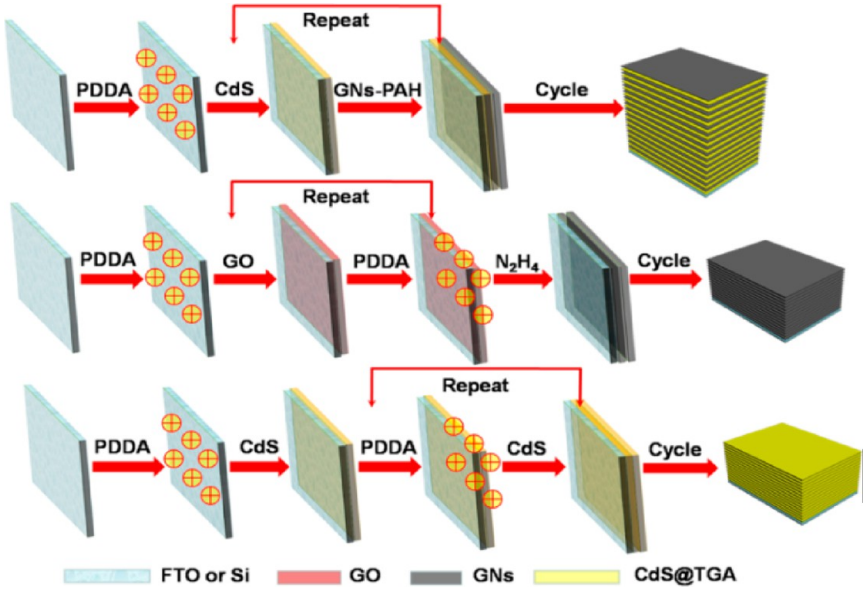

optical properties of CdS.[32−41] However, most of the synthetic protocols presented so far were based on conventional wet chemical approaches including hydrothermal,[40] solvothermal,[32,37,38] direct precipitation,[35] and sequential chemical bath deposition (CBD),[36] few of which have actually taken full advantage of 2D nanoarchitecture of GNs and guaranteed monodispersed deposition of CdS in nanometer regime on GNs. In addition, intimate integration of GNs with CdS in a well-defined architecture has been far from satisfactory, which may limit the great potentials of GNs−CdS heterostructures.

Herein, we develop a LBL self-assembly approach for the construction of GNs−CdS QDs composite films, in which positively charged GNs-PAH and negatively charged CdS QDs were employed as nanobuilding blocks for the self-assembly of well-defined GNs−CdS QDs multilayered films. The PAH modification exerts a profound influence on the charge transformation of GNs leading to positively charged surface, which acts as a robust scaffold for LbL self-assembly. It was found that the GNs−CdS QDs multilayered films exhibited promising photoelectrochemical and photocatalytic performances under visible light irradiation due to the intimate interfacial contact between CdS QDs and GNs. The origin accounting for the improved photoactivity and the underlying photocatalytic mechanism were also probed in this work. It is anticipated that our work will open new directions for the fabrication of various uniform semiconductor/GNs hybrid films for a wide range of applications.

2. EXPERIMENTAL SECTION

2.1. Materials. Fluorine-doped tin oxide (FTO) substrate, cadmium chloride ($CdCl_2·2.5H_2O$), sodium sulfide ($Na_2S·9H_2O$), thioglycolic acid ($C_2H_4O_2S$, TGA), poly(diallyldimethylammonium chloride) (PDDA, 1 mg/mL, 0.5 M NaCl, $M_w \approx 200\,000-350\,000$), poly(allylamine hydrochloride) (PAH, 1 mg/mL, 0.5 M NaCl, $M_w \approx 15\,000$ g mol^{-1}), graphite powder, sulfuric acid (H_2SO_4), nitric acid (HNO_3), hydrochloric acid (HCl), hydrogen peroxide (H_2O_2, 30%), potassium permanganate ($KMnO_4$), hydrazine (N_2H_4, 98%), deionized water (DI H_2O, Milipore, 18.2 MΩ cm resistivity), sodium chloride (NaCl), sodium hydroxide (NaOH), ammonium formate (HCO_2NH_4), potassium persulfate ($K_2S_2O_8$), 4-nitroaniline (4-NA), 3-nitroaniline (3-NA), 2-nitroaniline (2-NA), 1-chloro-4-nitrobenzene, 1-bromo-4-nitrobenzene, 4-nitrotoluene, 4-nitroanisole, and 4-nitrophenol were all of analytical grade and used as received without further purification.

2.2. Synthesis. *1. Synthesis of TGA-Stabilized CdS QDs (CdS@TGA QDs).* CdS QDs were synthesized according to previous reports with slight modifications.[42,43] Briefly, 250 μL of TGA was added to 50 mL of $CdCl_2$ (10 mM) aqueous solution, and N_2 was bubbled throughout the solution to remove O_2 at 110 °C. During this period, 1.0 M NaOH aqueous solution was slowly added to adjust the solution pH to 11. Following, 5.5 mL of 0.1 M Na_2S aqueous solution was injected to grow the TGA-capped water-soluble CdS QDs. The reaction mixture was refluxed under N_2 atmosphere for 4 h. Finally, the desired TGA-stabilized CdS QDs were synthesized and stored in a refrigerator at 4 °C for further use.

2. Synthesis of Graphite Oxides (GOs). GOs were synthesized from natural graphite sheets by a modified Hummers method.[44,45] The details of the synthetic process were provided in the Supporting Information.

3. Synthesis of GNs-PAH. The synthesis procedures are analogous to previous work with slight modifications.[10] GO was added into DI H_2O and ultrasonicated in an ultrasonic bath (Elmasonicator 30 H) for 8 h to form a stable dispersion (0.25 mg/mL). The resulting homogeneous GO aqueous solution (20 mL) was mixed with 20 mL of PAH aqueous solution (1.0 mg/mL, 0.5 M NaCl, pH = 4.5), and the mixed solution was stirred at 60 °C for 12 h. After being cooled to ambient temperature, 50 μL of N_2H_4 (98%) solution was added, and subsequently the reaction system was put in an oil bath at 95 °C for 12 h. After reaction, extra PAH and N_2H_4 were removed by centrifugation at 15 000*g* for 20 min, washed three times, and followed by redispersing in DI H_2O for further use.

4. LbL Self-Assembly of the GNs−CdS QDs Multilayered Films. The detailed assembly process was vividly illustrated in Scheme 1. FTO substrates were cleaned in a freshly prepared "piranha" solution (3:1 concentrated 98% H_2SO_4/30% H_2O_2; Caution: piranha solution reacts violently with organic materials and should be handled with great care) for 30 min, then rinsed with DI H_2O, and dried with a stream of N_2. The cleaned FTO substrate was rapidly dipped into PDDA aqueous solution (1.0 mg/mL, 0.5 M NaCl, pH = 8) for 20 min and washed three times with DI H_2O for 2 min, followed by drying with a gentle stream of N_2. Subsequently, the resultant substrate was immersed in TGA-capped CdS QDs aqueous solution for 20 min, rinsed with DI H_2O, and dried by a stream of N_2. Finally, the substrate was dipped into GNs-PAH aqueous solution (0.25 mg/mL) for 20 min and washed by DI H_2O and dried with N_2. The above procedure as a whole was designated as a single deposition cycle. Multilayered

dx.doi.org/10.1021/ja411651e | J. Am. Chem. Soc. 2014, 136, 1559−1569

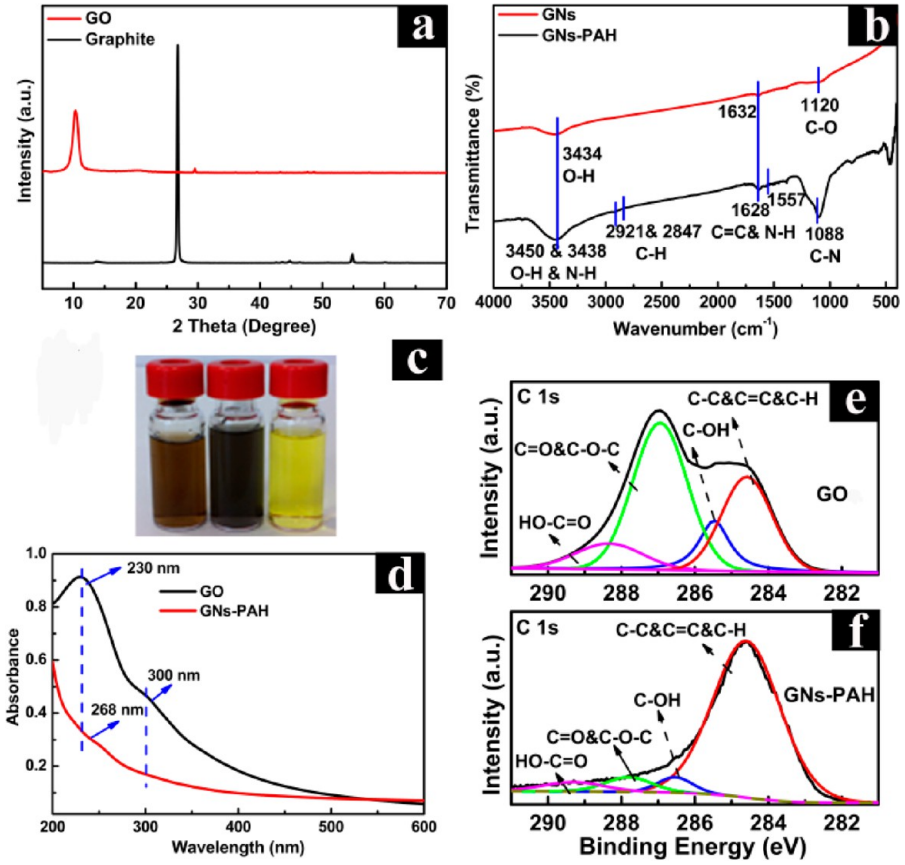

Figure 1. (a) XRD patterns of graphite and GO. (b) FTIR spectra of GNs-PAH and GNs prepared via reduction of GO under ambient conditions. (c) Photographs of GO (brown), GNs-PAH (black), and CdS QDs (yellow) aqueous solution. (d) UV−vis absorption spectra of GO and GNs-PAH aqueous solution. High-resolution XPS spectra of C 1s for (e) GO and (f) GNs-PAH.

films with desired film thickness were fabricated by repeating the number of dipping cycles. For comparison, pure CdS QDs film was prepared by alternating LbL self-assembly of PDDA and CdS QDs on FTO substrate, and pure GNs film was prepared by alternating LbL self-assembly of PDDA and GO on FTO substrate, followed by reduction via dipping into N_2H_4 solution under ambient conditions for 4 h.

2.3. Characterization. The phase composition of the sample was determined by X-ray diffraction (XRD) on a Bruker D8 Advance X-ray diffractometer with Cu Kα radiation. The accelerating voltage and applied current were 40 kV and 40 mA, respectively. X-ray photoelectron spectroscopy (XPS) measurements were conducted on an ESCALAB 250 photoelectron spectrometer (Thermo Fisher Scientific) at 2.4 × 10^{-10} mbar using a monochromatic Al Kα X-ray beam (1486.60 eV). All binding energies were referenced to the C 1s peak (284.60 eV) arising from adventitious hydrocarbons. The morphologies of the samples were measured by field emission scanning electron microscopy (FESEM, JEOL, JSM6701F) and atomic force microscopy (AFM, MFP3D microscope, Asylum Research). The AFM samples were prepared by dipping GO, GNs-PAH, GNs, or CdS QDs aqueous solution directly on the silicon wafers with a 300 nm SiO_2 top layer and characterized with a silicon cantilever operating in a tapping mode. FTIR spectra were recorded in the transmittance mode with a resolution of 4 cm^{-1} using a Perkin-Elmer FTIR spectrometer. The UV−vis diffuse reflectance spectra (DRS) were recorded on a Varian Cary 500 Scan UV−vis−NIR spectrometer, in which $BaSO_4$ was used as the background in the 200−800 nm range. The zeta potential of samples was determined by dynamic light scattering analysis (Zeta PALS, Brookhaven Instruments Co.). Transmission electron microscopy (TEM) images were obtained by a JEOL model JEM 2010 EX instrument at an accelerating voltage of 200 kV. Photoelectrochemical measurements were carried out in a homemade three-electrode quartz cell with electrochemical workstation (ZIVE SP2) in which platinum sheet was used as a counter electrode, Ag/AgCl electrode was used as a reference electrode, and the samples with active area of about 25 mm × 17 mm were used as the working electrodes. An aqueous Na_2S solution (0.1 M) was chosen as the electrolyte. A 300 W xenon arc lamp with an AM 1.5G filter (Newport) and a UV cutoff filter (λ > 420 nm) was applied as the light source.

2.4. Photocatalytic Activity. In a typical photocatalytic reaction, a 300 W xenon arc lamp with an AM 1.5G filter (Newport) and a UV cutoff filter (λ > 420 nm) was used for visible light irradiation. Specifically, the samples with active area of around 30 mm × 17 mm were immersed into 15 mL of aromatic nitro compounds aqueous solution (10 mg L^{-1}) in a quartz vial (55 mm × 54 mm × 14 mm) along with adding 20 mg of HCO_2NH_4. Before irradiation, the solution was stirred in the dark for 1 h to ensure the adsorption−desorption equilibrium between the sample and reactant. During the reaction process, 3 mL of sample solution was collected at a certain time interval and analyzed on a Varian UV−visible light spectrometer (Cary-50, Varian Co.). The whole experimental process was conducted under N_2 bubbling at ambient conditions. Conversion of the aromatic nitro compounds during the photocatalytic reaction was defined as follows:

$$\text{conversion}\ (\%) = [(C_0 - C)/C_0] \times 100$$

where C_0 is the initial concentration of aromatic nitro compounds, and C is the concentration of the substrate aromatic nitro compounds at a certain time interval after photocatalytic reaction.

dx.doi.org/10.1021/ja411651e | J. Am. Chem. Soc. 2014, 136, 1559−1569

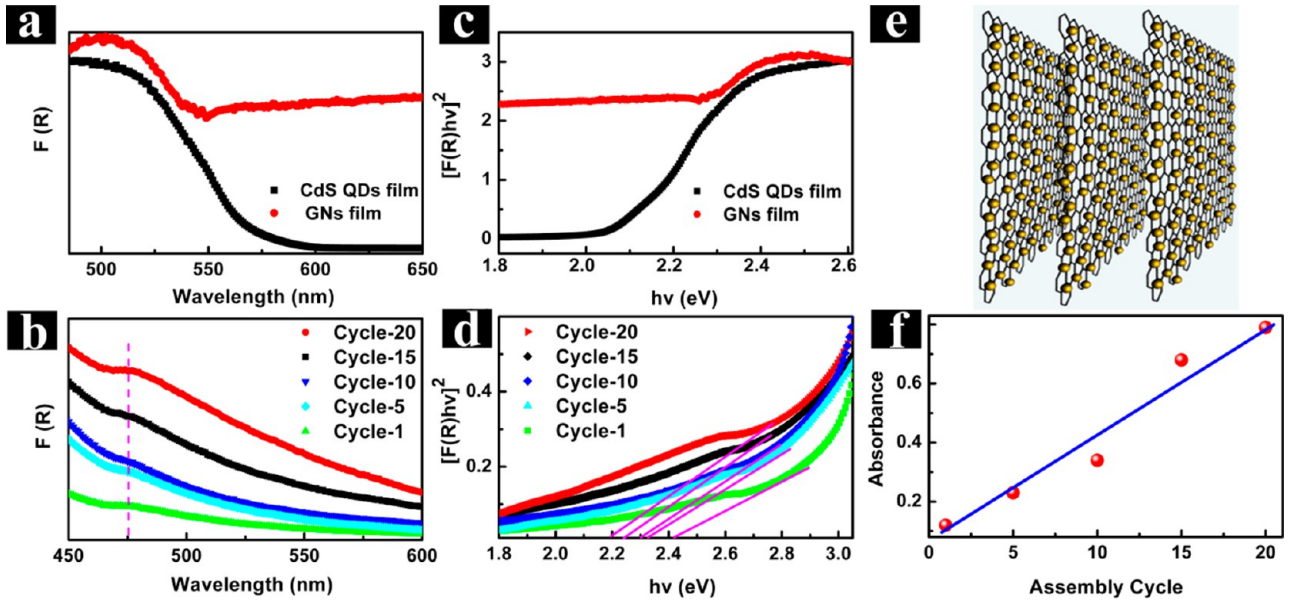

Figure 2. UV−vis absorption spectra of (a) pure CdS QDs and GNs films assembled after 5 deposition cycles, and (b) $(GNs−CdS\ QDs)_n$ (n = 1, 5, 10, 15, 20) multilayered films with varied deposition cycles. (c and d) Plot of transformed Kubelka−Munk function versus energy of light for (a) and (b), respectively. (e) Stacking model between CdS QDs and GNs-PAH. (f) Absorption of $(GNs−CdS\ QDs)_n$ multilayered films at wavelength of 475 nm versus the number of deposition cycles.

3. RESULTS AND DISCUSSION

In the LbL self-assembly process, electrostatic interaction between positively charged GNs-PAH and negatively charged CdS QDs was utilized as the core driving force for construction of the multilayered films. Surface charge properties of the nanobuilding blocks are displayed in Supporting Information Figures S1,S2, which show zeta potential values of −40, −45, and +43 mV, corresponding to CdS QDs, GO, and GNs-PAH, respectively. The pronounced positive zeta potential of GNs-PAH indicates successful charge transformation of GNs after PAH modification (Supporting Information Figure S2). It is important to mention that these zeta potentials are ideal for stabilizing colloidal particles in an aqueous solution, as defined by the American Society for Testing and Materials (ASTM).[46,47] As shown in Scheme 1, FTO substrate with negatively charged surface after "piranha" solution treatment was first modified by PDDA, which acts as the precursor film, and subsequently different layers of CdS QDs and GNs-PAH were deposited onto the precursor film to construct the $(GNs−CdS\ QDs)_n$ multilayered film, where n is the number of deposition cycles. It should be emphasized that in such a hybrid film, GNs-PAH and CdS QDs were stacked in an alternating manner with intimate interfacial contact, which would be beneficial for shuttling photogenerated electrons from CdS QDs to GNs. Meanwhile, to highlight the advantage of the $(GNs−CdS\ QDs)_n$ hybrid films, counterparts of pure GNs and CdS QDs films were also fabricated via analogous LbL self-assembly strategy (Scheme 1).

3.1. Synthesis of Nanobuilding Blocks for LbL Self-Assembly. GO was synthesized from natural graphite using a modified Hummers method. As shown in Figure 1a, the diffraction peak at 10.8° corresponds to GO (001) with interlay space (d-spacing) of around 0.8 nm, which is larger than the d-spacing (0.34 nm) of natural graphite (26.5°) due to trapping of approximately one-molecule-thick layer of water, suggesting complete exfoliation of oxidized GNs from graphite.[26,48] The typical 2D nanoflake structure of GO was evidenced by examining its morphology as shown in Supporting Information Figure S4. Figure 1c displays a homogeneous aqueous dispersion of GNs-PAH (black), which is rather stable without any precipitation even after several months storage under ambient conditions, indicating the reduced GO (i.e., GNs) was well-stabilized by PAH as a result of substantial electrostatic repulsion among positively charged PAH chains grafted on GNs. The reduction of GO as well as formation of GNs-PAH can be further corroborated by the FTIR results. As shown in Supporting Information Figure S5a, GO exhibits characteristic bands at 3410 and 1425, 1731, 1625, 1222, and 1051 cm^{-1}, which are ascribed to hydroxyl group (−OH), carbonyl group (C═O), aromatic bonds (C═C), epoxy group (C−O−C), and alkoxy group (C−OH and C−O), respectively.[49−51] When GO was reduced to GNs, there was a dramatic decrease or disappearance of the adsorption bands associated with oxygen-containing functional groups (Supporting Information Figure S5b). Meanwhile, a new peak at 1565 cm^{-1} appeared (Supporting Information Figure S5b), which can be attributed to typical skeletal vibration of GNs and is believed to result from restoration of the highly conjugated structure of GNs after chemical reduction.[52] Furthermore, with functionalization of GNs with PAH, a weak doublet at 2847 and 2921 cm^{-1} corresponding to symmetric V_s (CH_2) and asymmetric V_{as} (CH_2) of PAH chains appears (Figure 1b). The N−H bending vibration mode at 1628 and 1557 cm^{-1} together with C−N stretching mode at 1088 cm^{-1} concurrently verified successful attachment of PAH on GNs. Noteworthily, the very weak FTIR peaks associated with PAH (i.e., CH_2, N−H, C−N) indicate that only a small amount of PAH was grafted on GNs. The reduction of GO to GNs-PAH was ascertained by the sample's optical absorbance. As shown in Figure 1d, two absorption bands of GO located at 230 and 300 nm gradually disappear and shift to 268 nm during the reaction, which is typical for chemically reduced GO (i.e., GNs).[53,54] Additionally, XPS result (Figure 1e,f) shows that the intensity of hydroxyl and epoxy groups representing dominant oxygen-containing func-

dx.doi.org/10.1021/ja411651e | J. Am. Chem. Soc. 2014, 136, 1559−1569

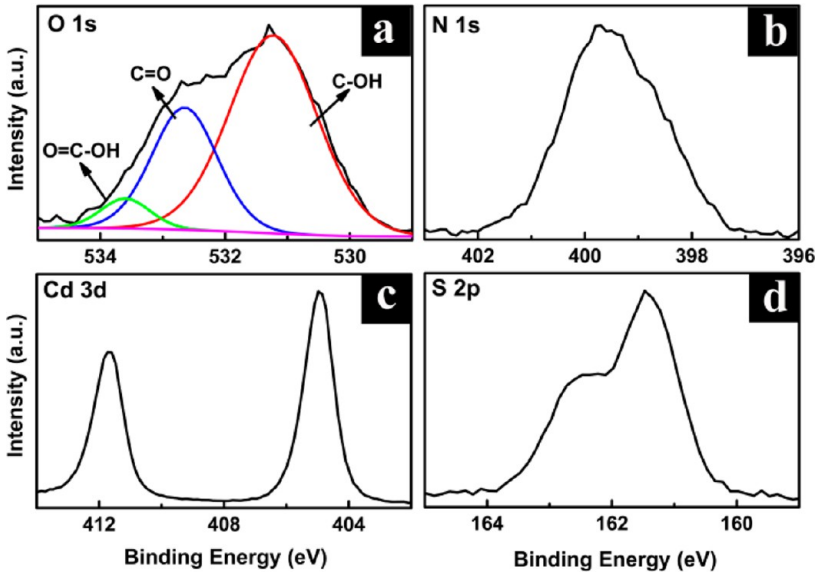

Figure 3. High-resolution XPS spectra of (a) O 1s, (b) N 1s, (c) Cd 3d, and (d) S 2p for $(GNs-CdS\ QDs)_5$ hybrid film.

tional groups of GO remarkably decreases, and simultaneously the intensity of sp^2 hybridized carbon increases, confirming the removal of oxygen-containing functional groups after chemical reduction.[52]

TGA-stabilized CdS QDs were synthesized using a solution chemical method. The detailed structural characterization of the TGA-stabilized CdS QDs was displayed in Supporting Information Figure S3.

3.2. LbL Self-Assembly of the GNs−CdS QDs Composite Films. UV−vis diffuse reflectance spectra (DRS) were used to probe the optical properties of the GNs, CdS QDs, and GNs−CdS QDs multilayered films. It can be seen from Figure 2a that pure CdS QDs and GNs multilayered films exhibit light absorbance extending to visible regime (>450 nm), which is in faithful agreement with the color of the samples (i.e., black for GNs film and yellow for CdS QDs film). Figure 2b shows DRS results of the $(GNs-CdS\ QDs)_n$ (n = 1, 5, 10, 15, 20) composite films, in which optical absorbance increases gradually with the number of assembly cycles, particularly that absorbance intensity of the composite films in the designated wavelength region (i.e., 450 nm < λ < 550 nm), corresponding to featured light absorbance of CdS QDs, increases proportionally to the number of deposition cycles, as illustrated in Figure 2f. The linear increase of CdS QDs absorbance as a function of assembly cycle strongly signifies uniform and cumulative self-assembly of CdS QDs in the $(GNs-CdS\ QDs)_n$ (n = 1, 5, 10, 15, 20) multilayered films (Figure 2e). A plot obtained via the transformation based on Kubelka−Munk function versus energy of light is shown in Figure 2c and d. The estimated bandgaps of the composite films are determined to be around 2.41, 2.36, 2.32, 2.24, and 2.20 eV, corresponding to hybrid films with assembly cycles of 1, 5, 10, 15, and 20, respectively. This result indicates a bandgap narrowing of CdS QDs when integrated with GNs by an alternating self-assembly in the $(GNs-CdS\ QDs)_n$ hybrid film (Figure 2e), which can be ascribed to interfacial interaction between CdS QDs and GNs.[5,41]

The compositional information and elemental chemical states of the $(GNs-CdS\ QDs)_n$ composite films were probed with X-ray photoelectron spectroscopy (XPS). Figure 3a displays the high-resolution XPS spectrum of O 1s in which three fitted peaks located at binding energies (BE) of 531.2, 532.6, and 533.6 eV are attributed to oxygen species of C−OH, C═O, and HO−C═O, respectively, grafted on the verge of GNs, demonstrating the integration of GNs in the multilayered films, which also agrees with the high-resolution XPS spectrum of C 1s in Figure 1f. The N 1s signal in Figure 3b arises primarily from the ultrathin PDDA layer adsorbed on the precursor film and PAH grafted on GNs, thus suggesting alternating deposition of GNs-PAH and CdS QDs via the linking network. As shown in Figure 3c, high-resolution spectrum of Cd 3d with featured peaks of 411.6 eV (Cd $3d_{3/2}$) and 404.9 eV (Cd $3d_{5/2}$) reveals the Cd element is in the +2 oxidation state (Cd^{2+}).[55] High-resolution spectrum of S 2p (Figure 3d) with BE of 161.88 eV (S $2p_{3/2}$) is ascribed to the hybrid chemical bond species of S^{2-} and Cd−S− arising from CdS@TGA,[56] confirming successful self-assembly of CdS QDs in the GNs−CdS QDs composite film.

Surface morphologies of the immobilized films self-assembled on FTO substrate were examined by field emission scanning electron microscopy (FESEM). Figure 4a reveals that GO nanosheets with a broad size distribution over several micrometers were uniformly spread on FTO substrate with high surface coverage. No obvious aggregation and irregular wrinkles of GO were observed (Supporting Information Figure S6). As displayed in Figure 4b, nanoflake structure of GNs after PAH modification was retained, and GNs-PAH were evenly distributed over large area on the substrate. Figure 4c shows the morphology of blank CdS QDs film, which exhibits a very flat surface homogenously distributed over the whole region of substrate (also see the low-magnified FESEM image in Supporting Information Figure S7). It should be pointed out that such a uniform and flat surface of CdS QDs layer would be beneficial for alternating self-assembly of GNs−CdS QDs composite films. The FESEM image of the GNs−CdS QDs composite film (Figure 4d) also demonstrated a dense and uniform surface, however, accompanied by much more rough surface as compared to pure GO and GNs-PAH films, which is attributed to uniform attachment of CdS QDs on the GNs-PAH under substantial electrostatic interaction.

dx.doi.org/10.1021/ja411651e | J. Am. Chem. Soc. 2014, 136, 1559−1569

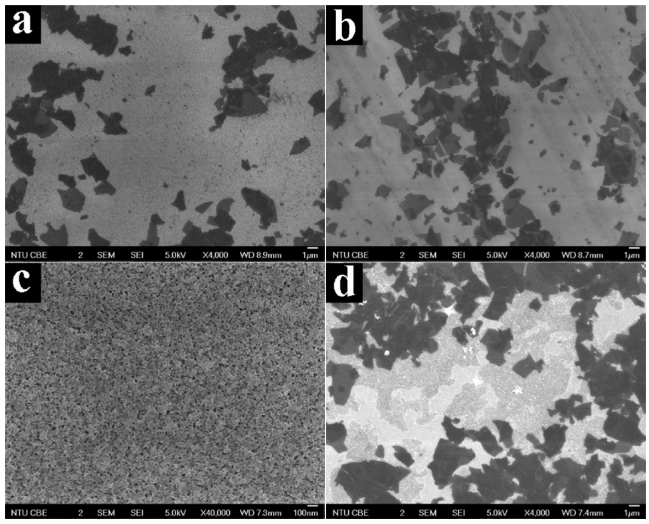

Figure 4. FESEM images of (a) pure GO, (b) GNs-PAH, (c) CdS QDs, and (d) $(GNs-CdS\ QDs)_5$ composite films self-assembled on FTO substrate with the same five deposition cycles.

AFM images of GO, GNs-PAH, CdS QDs film, and GNs–CdS QDs composite film are shown in Supporting Information Figures S8 and S9 and Figure 5. The AFM image of GNs-PAH (Supporting Information Figure S9) shows irregularly shaped individual sheets, ranging from several hundred nanometers to several micrometers. The measured sheet thickness of GNs-PAH is almost identical to that of exfoliated GO (1 to 1.5 nm, Supporting Information Figure S8), indicating that monolayer property of GNs was not affected by the integration of PAH modification. It is worthwhile to note that the surface of GNs-PAH was more rough than that of GO, which reflects grafting of PAH on flat GNs substrate. The magnified AFM image of CdS QDs film (Figure 5b) shows uniform distribution of CdS QDs with a tightly stacked morphology, which is in line with the FESEM result as shown in Figure 4c. As displayed in Figure 5d and e, AFM images of the $(GNs-CdS\ QDs)_5$ composite film reveal an interconnected structure between CdS QDs and GNs-PAH in which CdS QDs were intimately enclosed by GNs-PAH resulting in high surface coverage of QDs. Furthermore, 3D AFM images of CdS QDs and GNs–CdS QDs composite films were illustrated for comparison, as displayed in Figure 5c and f. Figure 5f shows that CdS QDs were closely and compactly enwrapped by GNs-PAH nanosheets on the top layer, which is remarkably distinct from the morphology of pure CdS QDs film (Figure 5c). Consequently, 3D AFM images strongly evidence the intimate integration of CdS QDs and GNs-PAH by LbL self-assembly buildup.

Transmission electron microscopy (TEM) images were further taken to discern the morphologies of GO, GNs-PAH, and GNs–CdS QDs hybrid film. As shown in Figure 6b, the TEM image of GNs-PAH is analogous to that of GO (Figure 6a), for both of which monolayer sheet with corrugated flake-like shape was clearly observed, and at the same time, restacked and wrinkle parts were also seen, which can be attributed to electronic repulsion between the soft and flexible layers.[57] Strikingly, Figure 6c–e and Supporting Information Figure S10 manifest that GNs-PAH was densely and homogeneously covered by monodispersed CdS QDs over the whole profile after the LbL self-assembly buildup, verifying efficient attachment of CdS QDs on the GNs-PAH. Noteworthily, loading density of CdS QDs on the GNs-PAH varies substantially with the deposition cycles, indicating the amount of CdS QDs during the LbL self-assembly process can be tuned by deposition cycles. In addition, the SAED pattern of the composite film (Figure 6f, inset) reveals polycrystalline nature of the hybrid film consisting of both CdS and graphene. Lattice spacing of 3.36 Å in Figure 6f was assigned to the (111) crystallographic plane of CdS QDs.

3.3. Photoelectrochemical Performances of the GNs–CdS QDs Hybrid Films. Photoelectrochemical measurements were carried out to study the role of interfacial contact between CdS QDs and GNs in GNs–CdS QDs composite films.[58,59] Figure 7a and Figure 7d show transient photocurrent responses for CdS QDs, GNs, and $(GNs-CdS\ QDs)_n$ (n = 1, 5, 10, 15, 20) multilayered films under visible light irradiation at zero bias condition. It is clear to see that the photocurrent of GNs–CdS QDs composite film was always larger than that of CdS QDs and GNs films with the same number of deposition cycles. The enhanced photoelectrochemical performances of GNs–CdS QDs composite films can be attributed to the alternating deposition between CdS QDs and GNs, which takes full advantage of 2D planar structure of GNs leading to the formation of intimate interfacial contact. In this way, photoexcited electrons in CdS QDs can be readily and efficiently transferred from the conduction band of CdS to the neighboring GNs scaffold upon visible light irradiation, where GNs serve as efficient electron collector and transporter, thus suppressing recombination of photogenerated electron–hole pairs. It is worthwhile to note that the photocurrent of the GNs–CdS QDs multilayered films first increases gradually with the number of deposition cycles, reaches a maximum at 15 cycles, and then decreases as the number of deposition cycles further increases. This trend is possibly caused by the competition of photon absorption between CdS QDs and GNs, which is corroborated by measuring the photocurrent of composite films with different stacking fashion as illustrated in Supporting Information Figures S11 and Figure S12. It was found that too much photon absorption by GNs (e.g., the second model in Supporting Information Figure S11 and the first model in Supporting Information Figure S12) significantly reduced the photocurrent of hybrid films. Simultaneously, the imperative role of intimate interfacial interaction between CdS QDs and GNs could also be highlighted by the photocurrent profiles of these composite films with different stacking patterns (Supporting Information Figure S11). Consequently, it is of great importance to balance photon absorption competition and interfacial contact between CdS QDs and GNs to achieve higher photocurrent for the multilayered films. Additionally, photocurrent as a function of applied voltage of CdS QDs and GNs–CdS QDs composite films with the same number of deposition cycle (5 or 15) was displayed in Figure 7b and e, which discloses significantly enhanced photocurrent for the composite film, thereby once again corroborating the contribution role of GNs for promoting separation of photogenerated electron–hole pairs.

Electrochemical impedance spectroscopy (EIS), a powerful tool to study charge transfer processes on the electrode and at the contact interface between electrode and electrolyte, was utilized to probe the separation efficiency of charge carriers.[60] In EIS Nyquist plot, the high frequency response comes from charge transfer at the Pt counter electrode, while the intermediate-frequency response is related to electron transport and transfer at the electrode–electrolyte interface.[61] The EIS Nyquist plots in Figure 7c and Figure 7f show that GNs–CdS

dx.doi.org/10.1021/ja411651e | J. Am. Chem. Soc. 2014, 136, 1559–1569

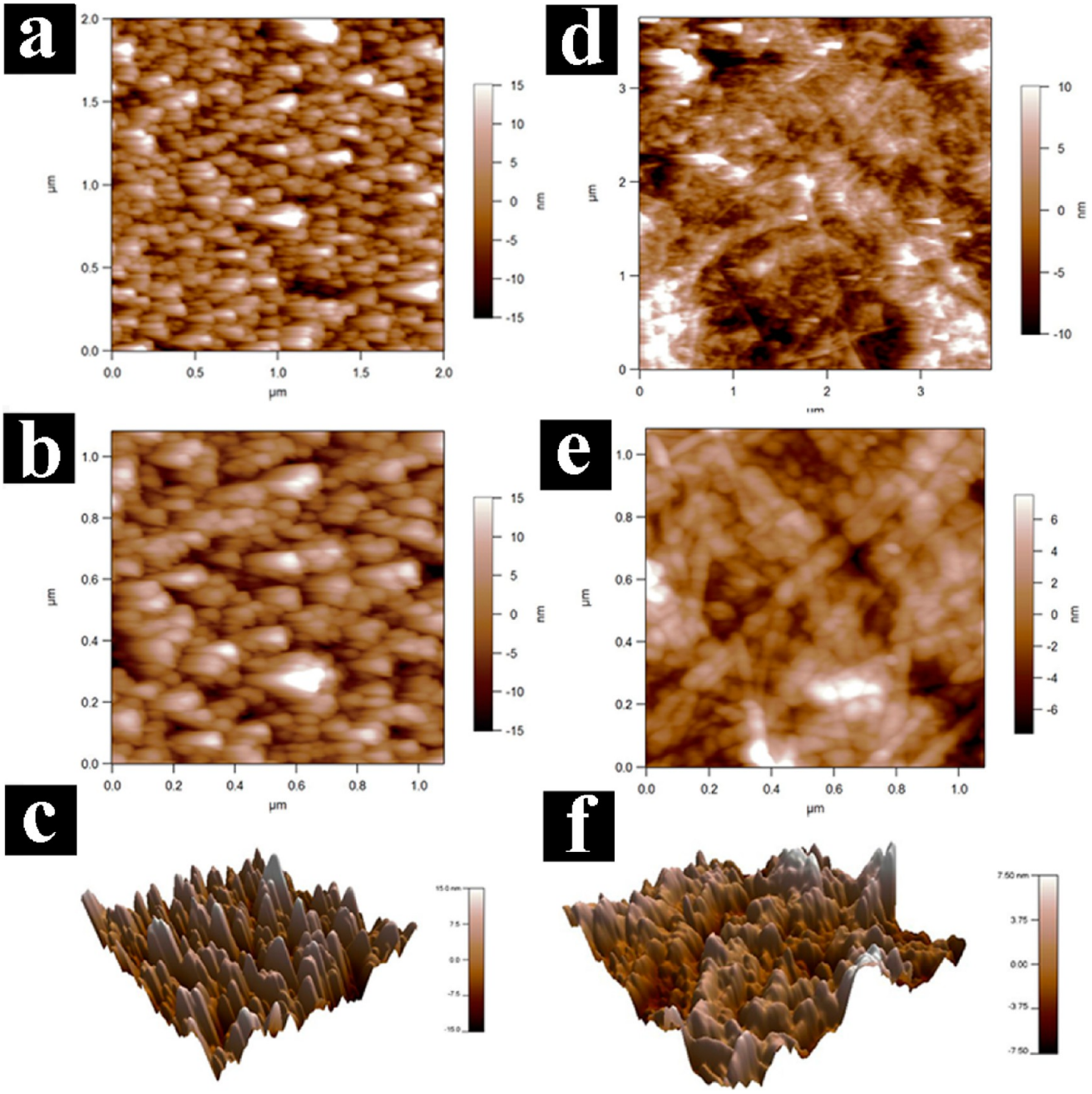

Figure 5. AFM images of (a,b) CdS QDs and (d,e) $(GNs–CdS\ QDs)_5$ composite films, and 3D AFM images of (c) CdS QDs and (f) $(GNs–CdS\ QDs)_5$ composite films assembled on silicon substrate.

QDs composite films have smaller semicircles in the intermediate-frequency region as compared to CdS QDs films with the same number of deposition cycles, which indicates more efficient interfacial electron transfer over the GNs–CdS QDs composite film. On the basis of the above photoelectrochemical (PEC) results, it is concluded that integration of GNs with CdS QDs based on LbL alternating deposition is beneficial for charge separation and transfer due to the 2D nanostructure and excellent conductivity of GNs, and, more importantly, the formation of intimate interfacial contact between CdS QDs and GNs. On the other hand, it is worth mentioning that PDDA sandwiched within pure CdS QDs film and PAH grafted on the verge of GNs were retained in the self-assembled system for PEC measurements, which suggests that PDDA and PAH, as conducting linking medium, did not significantly influence the shuttle and transport of photogenerated electrons. This can be attributed to the extremely thin adsorption layer of PDDA or PAH on the substrate (<1–2 nm), which is much less than the minority carrier diffusion length (>20 nm),[19,62,63] thus exerting negligible influence on the separation of photogenerated electron–hole charge carriers over CdS QDs film and GNs–CdS QDs multilayered film.[64–66] As shown in Supporting Information Figure S13, calcination of $(GNs–CdS\ QDs)_{15}$ composite film (300 °C, 0.5 h, N_2) demonstrated little effect on improving the photocurrent. Besides, it has been reported that PAH and PDDA can be oxidized during the photocatalytic process, hence contributing to the gradual improvement of the contact between neighboring components.[23,62,67,68] In this regard, it would be

dx.doi.org/10.1021/ja411651e | J. Am. Chem. Soc. 2014, 136, 1559–1569

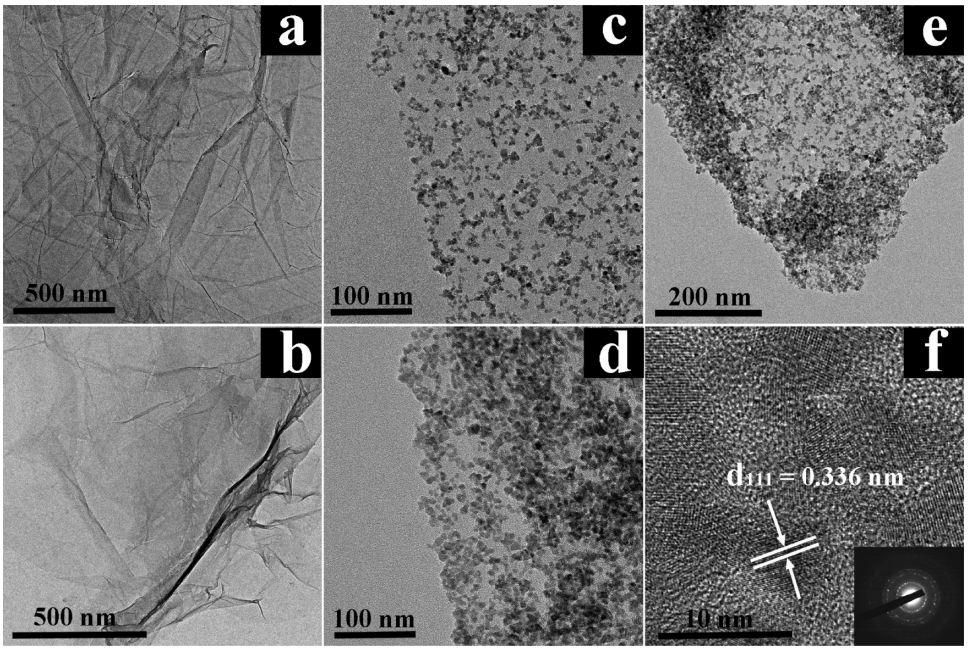

Figure 6. TEM images of (a) GO, (b) GNs-PAH, and GNs−CdS QDs composite film with (c) one and (d and e) five deposition cycles peeled off from FTO substrate, and (f) high-resolution TEM image of CdS QDs on the GNs-PAH with selected area electron diffraction (SAED) pattern in the inset.

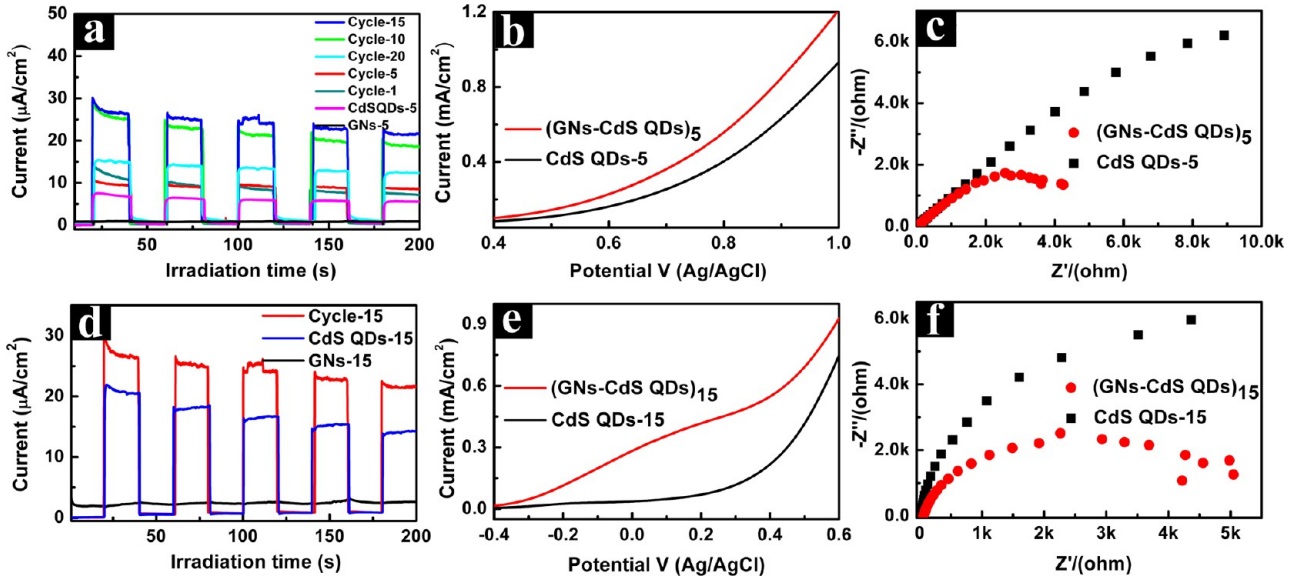

Figure 7. (a and d) Transient photocurrent responses of CdS QDs and GNs films with the same number of deposition cycles (5 or 15), and $(GNs−CdS\ QDs)_n$ (n = 1, 5, 10, 15, 20) multilayered films. (b and e) Photocurrent−voltage curves and (c and f) electrochemical impedance spectroscopy (EIS) Nyquist plots of CdS QDs film and GNs−CdS QDs multilayered film with the same number of deposition cycles (5 or 15) in 0.1 M Na_2S aqueous solution at zero bias versus Pt counter electrode under visible light irradiation (λ > 420 nm); the scanning rate is 100 mV/s, the amplitude of the sinusoidal wave was set at 10 mV, and the frequency varied from 100 kHZ to 0.05 HZ.

interesting to directly apply the self-assembled GNs−CdS QDs hybrid films for photorelated applications.

3.4. Photocatalytic Performances of the GNs−CdS QDs Hybrid Films. Photocatalytic performances of the CdS QDs film and GNs−CdS QDs composite films were evaluated by photoreduction of nitroaromatic compounds to corresponding amino organics in aqueous phase under visible light irradiation.[69−74] Blank experiments (without light or catalyst) under identical experimental conditions demonstrate negligible photoactivity, suggesting the reaction was driven by the photocatalytic process (Supporting Information Figure S14). As shown in Figure 8, the as-assembled GNs−CdS QDs hybrid film and its calcined counterpart exhibit remarkably enhanced photoactivity in comparison with CdS QDs film with the same number of deposition cycles toward reduction of nitroaromatic compounds to corresponding amino organics under visible light irradiation. The photocatalytic performances of the samples follow the order of: calcined GNs−CdS QDs composite film > as-assembled GNs−CdS QDs hybrid film > CdS QDs film, which emphasizes the importance of integration of CdS QDs

dx.doi.org/10.1021/ja411651e | J. Am. Chem. Soc. 2014, 136, 1559−1569

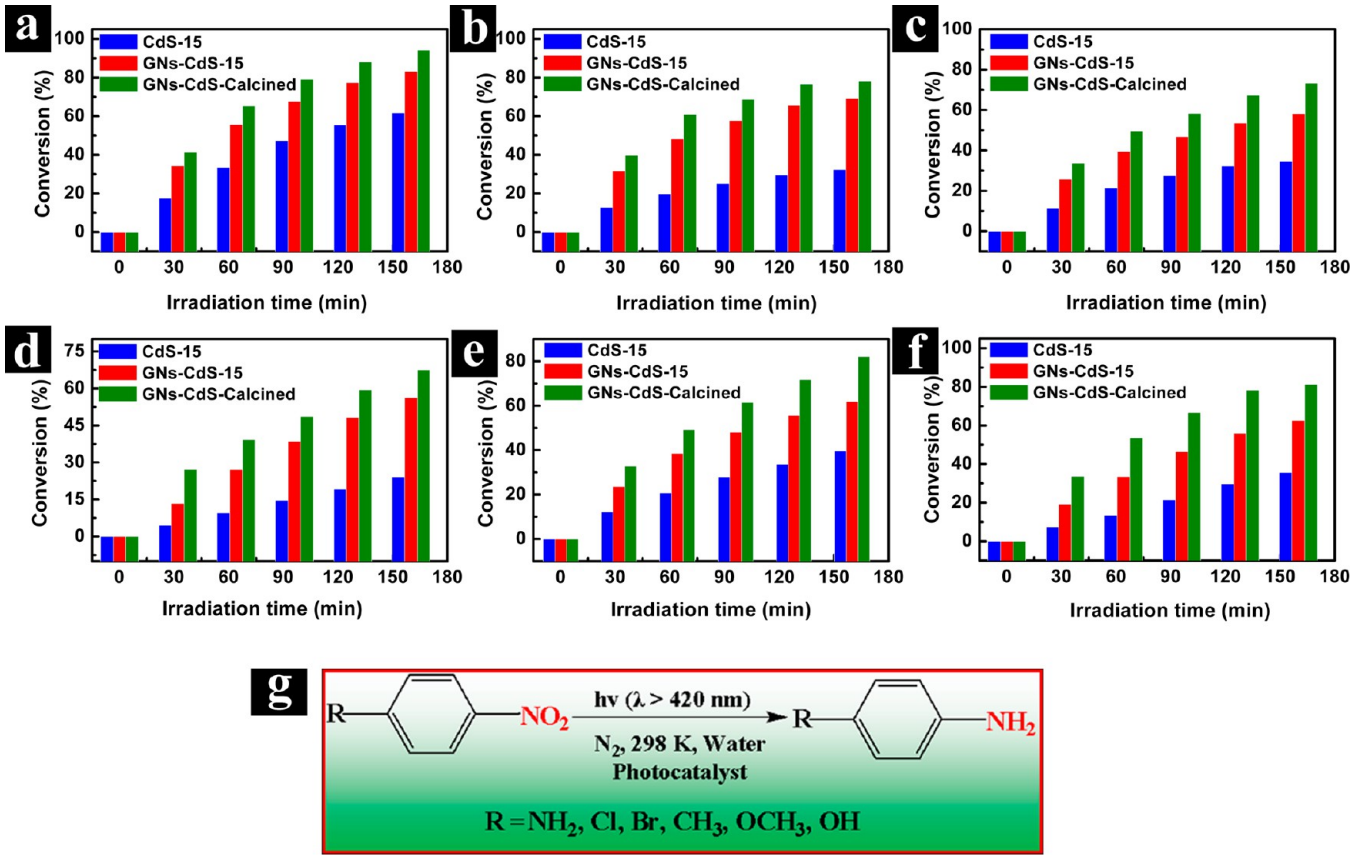

Figure 8. Photocatalytic reduction of substituted aromatic nitro compounds over CdS QDs film (15 cycles), as-assembled GNs−CdS QDs composite film (15 cycles), and calcined GNs−CdS QDs composite films (15 cycles) under visible light irradiation ($\lambda > 420$ nm), with the addition of ammonium formate as quencher for photogenerated holes and N_2 purge under ambient conditions: (a) 4-nitroaniline, (b) 1-chloro-4-nitrobenzene, (c) 1-bromo-4-nitrobenzene, (d) 4-nitrotoluene, (e) 4-nitroanisole, and (f) 4-nitrophenol. (g) Photocatalytic reduction model under the experimental conditions.

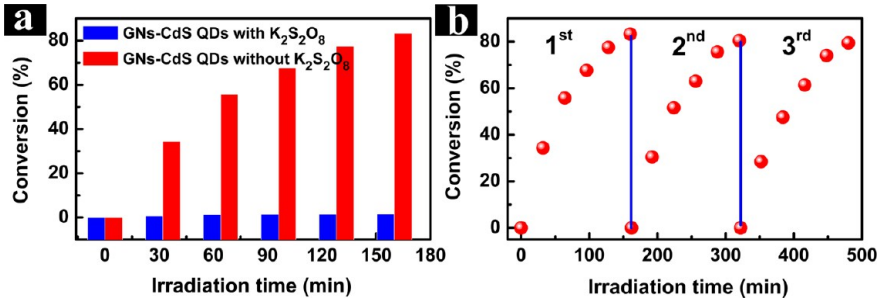

Figure 9. (a) Control experiments using $K_2S_2O_8$ as electron scavenger for reduction of 4-NA over GNs−CdS QDs hybrid film (15 cycles) under visible light irradiation ($\lambda > 420$ nm) with the addition of ammonium as quencher for photogenerated holes and N_2 purge under ambient conditions. (b) Cycling measurements of photocatalytic reduction of 4-NA over GNs−CdS QDs composite film under the same experimental conditions.

with GNs. Moreover, it is worthwhile to mention that photocatalytic performance of the composite film was improved to some extent after annealing treatment in an inert environment, which can be ascribed to better intimate interfacial contact between GNs and CdS QDs by attenuating the steric effect caused by PAH chains grafted on the verge of GNs framework. In addition, with respect to the reduction reactions under visible light irradiation, photocatalytic reduction of 4-nitroaniline (4-NA) to 4-phenylenediamine (4-PDA) over the CdS QDs film was presented as a typical example, which was monitored by the UV−vis light absorption spectra.[71] As shown in Supporting Information Figure S15, prior to visible light irradiation, only one absorption peak at 380 nm corresponding to 4-NA was observed. Two new peaks at ca. 300 and 240 nm gradually arose with the progress of reaction, which are attributed to the formation of 4-PDA, indicating the successful reduction of 4-NA to 4-PDA. The products of this reduction reaction under visible light irradiation have been ascertained by high performance liquid chromatography (HPLC). Notably, such a similar photoactivity enhancement trend has also been observed in other nitroaromatic compounds under the same visible light irradiation, such as 1-chloro-4-nitrobenzene, 1-bromo-4-nitrobenzene, 4-nitrotoluene, 4-nitroanisole, 4-nitrophenol, and homologues of 4-NA (e.g., 3-NA and 2-NA), as shown in Figure 8b−f and Supporting Information Figure S16.

dx.doi.org/10.1021/ja411651e | J. Am. Chem. Soc. 2014, 136, 1559−1569

To understand the role of photogenerated electrons for photocatalytic reduction of nitro compounds, control experiments with and without addition of $K_2S_2O_8$ as an electron scavenger for photogenerated electrons in N_2 atmosphere were carried out. As shown in Figure 9a, photocatalytic reduction of 4-NA over GNs−CdS QDs composite film was remarkably retarded when $K_2S_2O_8$ was introduced into the reaction system, which highlights the crucial role of photogenerated electrons in driving the photocatalytic reduction of aromatic nitro compounds. During the three successive recycling tests period, GNs−CdS QDs composite film exhibited persistent high photoactivity and good photostability (Figure 9b and Supporting Information Figure S17). In addition, it is worth noting that the use of GNs−CdS QDs composite film as photocatalyst could avoid the tedious catalyst separation procedure after photoreaction, which affords inimitable advantage over powder photocatalyst.

3.5. Photoelectrochemical and Photocatalytic Mechanisms over the GNs−CdS QDs Hybrid Films. Figure 10

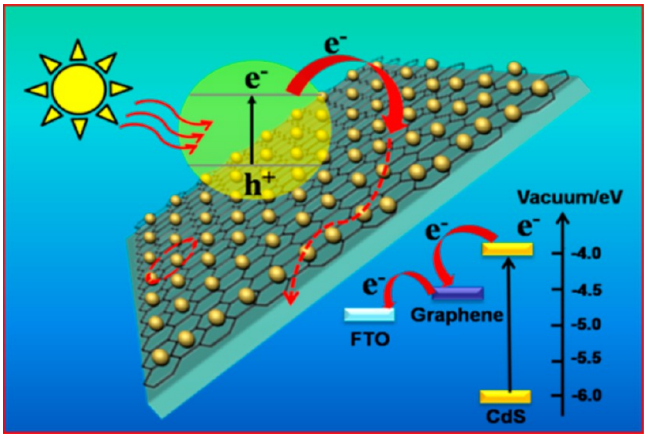

Figure 10. Schematic illustration of the PEC mechanism over the GNs−CdS QDs multilayered films.

and Supporting Information Figure S18 depict the PEC and photocatalytic mechanisms for the GNs−CdS QDs composite film. On the basis of previous work, the work function for GNs is ca. 4.42 eV,[75,76] and that for FTO substrate is known to be around 4.4 eV.[77] Meanwhile, CdS QDs with diameter of about 5.6 nm possess a conducting band (CB) at ca. −3.8 eV and a band gap of approximately 2.25 eV.[78] Hence, the energy-level diagram of the GNs−CdS QDs hybrid system was shown in the inset of Figure 10, from which it is clear to see that CB of CdS QDs is located above the work function of GNs, indicating favorable charge transfer from the CB of CdS QDs to GNs upon visible light excitation. The photoexcited electrons captured by GNs can be further readily transferred to FTO substrate, thus fulfilling separation of photogenerated electron−hole charge carriers and producing photocurrent. On the other hand, with regard to reduction of nitro compounds over the GNs−CdS QDs composite system under visible light irradiation (Supporting Information Figure S18), photoexcited holes from the valence band (VB) of CdS QDs are completely quenched by the addition of ammonium formate, and the photogenerated electrons from the CB of CdS QDs flow to GNs and react efficiently with the nitro compounds adsorbed on the GNs, thereby fulfilling the photoreduction process. Moreover, it should be noted that the reaction was carried out under N_2 purge, which prohibits the involvement of O_2 in the reaction system and guarantees the complete reduction of nitroaromatic compounds by the photogenerated electrons.

4. CONCLUSIONS

We have demonstrated a facile LbL self-assembly approach for the construction of well-defined GNs−CdS QDs multilayered films. These composite films are composed of tailor-made negatively charged CdS QDs and positively charged GNs-PAH, which are judiciously stacked in an alternating manner based on pronounced electrostatic interaction; by this means, large area, smooth, and uniform hybrid films were thus fabricated. It was found that the as-assembled GNs−CdS QDs multilayered films demonstrated promising photoelectrochemical and photocatalytic performances under visible light irradiation. The performance enhancement was attributed to the judicious integration of CdS QDs with GNs in an alternative stacking manner, which maximizes the charge separation and transport in GNs−CdS QDs composite film. It is anticipated that our work could open new directions for the fabrication of various uniform semiconductor/GNs hybrid films for a wide range of applications.

■ ASSOCIATED CONTENT

Supporting Information

Experimental section for the preparation of GO. Zeta potential of GO, CdS@TGA, and GNs-PAH. Structural characterization of CdS@TGA. Cross-sectional FESEM of GO. FTIR of GO and GNs. FESEM images of GNs and CdS QDs on FTO substrate. AFM images of GO and GNs-PAH with corresponding height profile. TEM images of GNs−CdS QDs composite film. Photoelectrochemical performances of GNs−CdS QDs composite films with different deposition fashions. Photoelectrochemical properties of calcined GNs−CdS QDs composite film. Blank experiments for photocatalytic reaction. UV−vis spectral variation for 4-NA. Photocatalytic reduction of nitroaniline over GNs−CdS QDs composite film. High-resolution XPS spectrum of Cd 3d. Schematic illustration for photocatalytic reduction mechanism. This material is available free of charge via the Internet at http://pubs.acs.org.

■ AUTHOR INFORMATION

Corresponding Author

liubin@ntu.edu.sg

Notes

The authors declare no competing financial interest.

■ ACKNOWLEDGMENTS

This work was supported by the Nanyang Technological University startup grant M4080977.120, Singapore Ministry of Education Academic Research Fund (AcRF) Tier 1: M4011021.120, and Singapore-Berkeley Research Initiative for Sustainable Energy (SinBeRise).We thank Dr. Fang Zhanxi and Prof. Zhang Hua for their kind help with TEM measurements.

■ REFERENCES

(1) Novoselov, K. S.; Geim, A. K.; Morozov, S. V.; Jiang, D.; Zhang, Y.; Dubonos, S. V.; Grigorieva, I. V.; Firsov, A. A. *Science* **2004**, *306*, 666.

(2) Su, Q.; Pang, S. P.; Alijani, V.; Li, C.; Feng, X. L.; Muellen, K. *Adv. Mater.* **2009**, *21*, 3191.

(3) Zhang, Y. H.; Zhang, N.; Tang, Z.-R.; Xu, Y.-J. *ACS Nano* **2012**, *6*, 9777.
(4) Zhang, Y. H.; Tang, Z.-R.; Fu, X. Z.; Xu, Y.-J. *ACS Nano* **2011**, *5*, 7426.
(5) Zhang, Y. H.; Tang, Z.-R.; Fu, X. Z.; Xu, Y.-J. *ACS Nano* **2010**, *4*, 7303.
(6) Stankovich, S.; Dikin, D. A.; Dommett, G. H. B.; Kohlhaas, K. M.; Zimney, E. J.; Stach, E. A.; Piner, R. D.; Nguyen, S. T.; Ruoff, R. S. *Nature* **2006**, *442*, 282.
(7) Gilje, S.; Song, H.; Wang, M.; Wang, K. L.; Kaner, R. B. *Nano Lett.* **2007**, *7*, 3394.
(8) Wang, X.; Zhi, L.; Mullen, K. *Nano Lett.* **2008**, *8*, 323.
(9) Schedin, F.; Geim, A. K.; Morozov, S. V.; Hill, E. W.; Blake, P.; Katsnelson, M. I.; Novoselov, K. S. *Nat. Mater.* **2007**, *6*, 652.
(10) Yu, D. S.; Dai, L. M. *J. Phys. Chem. Lett.* **2010**, *1*, 467.
(11) Li, D.; Muller, M. B.; Gilje, S.; Kaner, R. B.; Wallace, G. G. *Nat. Nanotechnol.* **2008**, *3*, 101.
(12) Wu, Z. S.; Pei, S.; Ren, W.; Tang, D.; Gao, L.; Liu, B.; Li, F.; Liu, C.; Cheng, H. M. *Adv. Mater.* **2009**, *21*, 1756.
(13) Li, X. L.; Zhang, G. Y.; Bai, X. D.; Sun, X. M.; Wang, X. R.; Wang, E.; Dai, H. *Nat. Nanotechnol.* **2008**, *3*, 538.
(14) Xu, Y.; Bai, H.; Lu, G.; Li, C.; Shi, G. *J. Am. Chem. Soc.* **2008**, *130*, 5856.
(15) Cai, D.; Song, M.; Xu, C. *Adv. Mater.* **2008**, *20*, 1706.
(16) Gilje, S.; Han, S.; Wang, M.; Wang, K. L.; Kaner, R. B. *Nano Lett.* **2007**, *7*, 3394.
(17) Wang, X.; Zhi, L.; Mullen, K. *Nano Lett.* **2008**, *8*, 323.
(18) Liang, Y. Y.; Zhi, L. J.; Norouzi-Arasi, H.; Feng, X. L.; Mullen, K. *Nanotechnology* **2009**, *20*, 434001.
(19) Decher, G. *Science* **1997**, *277*, 1232.
(20) Caruso, F.; Caruso, R. A.; Mohwald, H. *Science* **1998**, *282*, 1111.
(21) Cho, J.; Quinn, J. F.; Caruso, F. *J. Am. Chem. Soc.* **2004**, *126*, 2270.
(22) Xiao, F. *J. Phys. Chem. C* **2012**, *116*, 16487.
(23) Li, H. L.; Pang, S. P.; Wu, S.; Feng, X. L.; Mullen, K.; Bubeck, C. *J. Am. Chem. Soc.* **2011**, *133*, 9423.
(24) Zhao, X.; Zhang, Q.; Hao, Y.; Li, Y.; Fang, Y.; Chen, D. *Macromolecules* **2010**, *43*, 9411.
(25) Shen, J.; Hu, Y.; Li, C.; Qin, C.; Shi, M.; Ye, M. *Langmuir* **2009**, *25*, 6122.
(26) Liu, W.-W.; Yan, X.-B.; Xue, Q.-J. *J. Mater. Chem. C* **2013**, *1*, 1413.
(27) Zhang, N.; Zhang, Y.; Xu, Y.-J. *Nanoscale* **2012**, *4*, 5792.
(28) Zhang, N.; Yang, M.-Q.; Tang, Z.-R.; Xu, Y.-J. *ACS Nano* **2013**, DOI: 10.1021/nn405242t.
(29) Zhang, Y. H.; Zhang, N.; Tang, Z.-R.; Xu, Y.-J. *Chem. Sci.* **2012**, *3*, 2812.
(30) Zhang, Y. H.; Zhang, N.; Tang, Z.-R.; Xu, Y.-J. *Chem. Sci.* **2013**, *4*, 1820.
(31) Zhang, Y. H.; Zhang, N.; Tang, Z.-R.; Xu, Y.-J. *Phys. Chem. Chem. Phys.* **2012**, *14*, 9167.
(32) Li, Q.; Guo, B.; Yu, J.; Ran, J.; Zhang, B.; Yan, H.-J.; Gong, J. R. *J. Am. Chem. Soc.* **2011**, *133*, 10878.
(33) Jia, L.; Wang, D.-H.; Huang, Y.-X.; Xu, A.-W.; Yu, H.-Q. *J. Phys. Chem. C* **2011**, *115*, 11466.
(34) Zhang, N.; Yang, M.-Q.; Tang, Z.-R.; Xu, Y.-J. *J. Catal.* **2013**, *303*, 60.
(35) Cao, A.; Liu, Z.; Chu, S.; Wu, M.; Ye, Z.; Cai, Z.; Chang, Y.; Wang, S.; Gong, Q.; Liu, Y. *Adv. Mater.* **2010**, *22*, 103.
(36) Chang, H.; Lv, X.; Zhang, H.; Li, J. *Electrochem. Commun.* **2010**, *12*, 483.
(37) Guo, C. X.; Yang, H. B.; Sheng, Z. M.; Lu, Z. S.; Song, Q. L.; Li, C. M. *Angew. Chem., Int. Ed.* **2010**, *49*, 3014.
(38) Dufaux, T.; Boettcher, J.; Burghard, M.; Kern, K. *Small* **2010**, *6*, 1868.
(39) Wang, P.; Jiang, T.; Zhu, C.; Zhai, Y.; Wang, D.; Dong, S. *Nano Res.* **2010**, *3*, 794.
(40) Nethravathi, C.; Nisha, T.; Ravishankar, N.; Shivakumara, C.; Rajamathi, M. *Carbon* **2009**, *47*, 2054.
(41) Zhang, N.; Zhang, Y. H.; Pan, X. Y.; Fu, X. Z.; Liu, S. Q.; Xu, Y.-J. *J. Phys. Chem. C* **2011**, *115*, 23501.
(42) Zhao, W.-W.; Ma, Z.-Y.; Yu, P.-P.; Dong, X.-Y.; Xu, J.-J.; Chen, H.-Y. *Anal. Chem.* **2012**, *84*, 917.
(43) Wang, G. L.; Yu, P. P.; Xu, J.-J.; Chen, H.-Y. *J. Phys. Chem. C* **2009**, *113*, 11142.
(44) Hummers, W. S.; Offeman, R. E. *J. Am. Chem. Soc.* **1958**, *80*, 1339.
(45) Cote, L. J.; Kim, F.; Huang, J. *J. Am. Chem. Soc.* **2008**, *131*, 1043.
(46) Si, Y. C.; Samulski, E. T. *Nano Lett.* **2008**, *8*, 1679.
(47) Li, L.-L; Liu, K.-P; Yang, G.-H; Wang, C.-M; Zhang, J.-R; Zhu, J.-J. *Adv. Funct. Mater.* **2011**, *21*, 869.
(48) Liu, W.-W.; Yan, X. B.; Lang, J. W.; Xue, Q.-J. *J. Mater. Chem.* **2012**, *22*, 8853.
(49) Zhu, M. S.; Chen, P. L.; Liu, M. H. *ACS Nano* **2011**, *5*, 4529.
(50) Zhang, D.-D.; Zu, S.-Z.; Han, B.-H. *Carbon* **2009**, *47*, 2993.
(51) Titelman, G. I.; Gelman, V.; Bron, S.; Khalfin, R. L.; Cohen, Y.; Bianco-Peled, H. *Carbon* **2005**, *43*, 641.
(52) Zhang, L. B.; Chen, G. Y.; Hedhili, M. N.; Zhang, H. N.; Wang, P. *Nanoscale* **2012**, *4*, 7038.
(53) Liu, J. B.; Fu, S. H.; Yuan, B.; Li, Y. L.; Deng, Z. X. *J. Am. Chem. Soc.* **2010**, *132*, 7279.
(54) Kong, B. S.; Geng, J. X.; Jung, H. T. *Chem. Commun.* **2009**, *16*, 2174.
(55) Zhang, J.; Yu, J. G.; Jaroniec, M.; Gong, J. R. *Nano Lett.* **2012**, *12*, 4584.
(56) Nakanishi, T.; Ohtani, B.; Shimazu, K.; Uosaki, K. *Chem. Phys. Lett.* **1997**, *278*, 233.
(57) Huang, X.; Qi, X. Y.; Boey, F.; Zhang, H. *Chem. Soc. Rev.* **2012**, *41*, 666.
(58) Ng, Y. H.; Lwase, A.; Kudo, A.; Amal, R. *J. Phys. Chem. Lett.* **2010**, *1*, 2607.
(59) Manga, K. K.; Zhou, Y.; Yan, Y. L.; Loh, K. P. *Adv. Funct. Mater.* **2009**, *19*, 3638.
(60) Li, N.; Liu, G.; Zhen, C.; Li, F.; Zhang, L. L.; Cheng, H. M. *Adv. Funct. Mater.* **2011**, *21*, 1717.
(61) Jana, A.; Bhattacharya, C.; Datta, J. *Electrochim. Acta.* **2010**, *55*, 6553.
(62) Caruso, F.; Shi, X. Y.; Caruso, R. A.; Susha, A. *Adv. Mater.* **2001**, *13*, 740.
(63) Guo, Y.-G.; Wan, L.-J.; Bai, C.-L. *J. Phys. Chem. B* **2003**, *107*, 5441.
(64) Grimes, C. A.; Mor, G. K. *TiO_2 Nanotube Arrays Synthesis, Properties, and Applications*; Springer: Berlin, 2009.
(65) Allam, N. K.; Alamgir, F.; El-Sayed, M. A. *ACS Nano* **2010**, *4*, 5819.
(66) Chen, D.; Wang, G.; Lu, W.; Zhang, H.; Li, J. H. *Electrochem. Commun.* **2007**, *9*, 2151.
(67) Sasaki, T.; Ebina, Y.; Fukuda, K.; Tanaka, T.; Harada, M.; Watanabe, M. *Chem. Mater.* **2002**, *14*, 3524.
(68) Yao, H.-B.; Wu, L.-H.; Cui, C.-H.; Fang, H.-Y.; Yu, S.-H. *J. Mater. Chem.* **2010**, *20*, 5190.
(69) Zhang, N.; Xu, Y.-J. *Chem. Mater.* **2013**, *25*, 1979.
(70) Liu, S. Q.; Chen, Z.; Zhang, N.; Tang, Z.-R.; Xu, Y.-J. *J. Phys. Chem. C* **2013**, *117*, 8251.
(71) Liu, S. Q.; Xu, Y.-J. *Nanoscale* **2013**, *5*, 9330.
(72) Yang, M.-Q.; Weng, B.; Xu, Y.-J. *Langmuir* **2013**, *29*, 10549.
(73) Yang, M.-Q.; Xu, Y.-J. *Phys. Chem. Chem. Phys.* **2013**, *15*, 19102.
(74) Weng, B.; Liu, S. Q.; Zhang, N.; Tang, Z.-R.; Xu, Y.-J. *J. Catal.* **2014**, *309*, 146.
(75) Liu, Z. F.; Liu, Q.; Huang, Y.; Ma, Y. F.; Yin, S. G.; Zhang, X. Y.; Sun, W.; Chen, Y. S. *Adv. Mater.* **2008**, *20*, 3924.
(76) Czerw, R.; Foley, B.; Tekleab, D.; Rubio, A.; Ajayan, P. M.; Carroll, D. L. *Phys. Rev. B* **2002**, *66*, 033408.
(77) Helander, M. G.; Greiner, M. T.; Wang, Z. B.; Tang, W. M.; Lu, Z. H. *J. Vac. Sci. Technol., A* **2011**, *29*, 011019.
(78) Lee, H.; Leventis, H. C.; Moon, S. J.; Chen, P.; Ito, S.; Haque, S. A.; Torres, T.; Nuesch, F.; Geiger, T.; Zakeeruddin, S. M.; Gratzel, M.; Nazeeruddin, M. K. *Adv. Funct. Mater.* **2009**, *19*, 2735.